RSC Advances

PAPER

Cite this: *RSC Adv.*, 2014, **4**, 42412

Synthesis of nitrogen-doped reduced graphene oxide directly from nitrogen-doped graphene oxide as a high-performance lithium ion battery anode†

Meng Du, Jing Sun,* Jie Chang, Fan Yang, Liangjing Shi and Lian Gao

Received 10th June 2014
Accepted 2nd September 2014

DOI: 10.1039/c4ra05544f

www.rsc.org/advances

A new route has been developed to synthesize nitrogen-doped reduced graphene oxide (N-RGO) with excellent lithium storage properties. Nitrogen-doped graphene oxide (N-GO) is firstly synthesized and then reduced to N-RGO. The nitrogen content of N-GO can reach up to 5.6 wt%. After hydrothermal treatment, the nitrogen content of N-RGO still remains at 2.0 wt%. Our N-RGO material reveals excellent reversible capacity of 600 mA h g^{-1} at a current density of 0.1 C (1 C = 372 mA g^{-1}) after 60 cycles, superior to that of pristine-RGO (350 mA h g^{-1} at a current density of 0.1 C). Our work opens up a new way to synthesize N-RGO, which is a promising candidate for lithium ion battery (LIB) anodes. In addition, the intermediate N-GO, with high activity, can combine with other materials for convenient application. In this work the Fe_2O_3/N-RGO composite is also prepared to show the outstanding properties of N-RGO.

1. Introduction

Rechargeable LIBs as important types of power sources have been greatly used for popular consumer electronics. They are also considered to be the most promising batteries for hybrid electric vehicles.[1–4] Carbon materials are widely used as commercial LIB anodes for their outstanding cycling stability. Since the materials suffer from poor reversible capacity new breakthroughs need to be pursued intensively in anode electrode materials to achieve higher capacities.[5,6] Graphene, due to its huge surface area, high thermal conductivity, fast charged carrier mobility and strong Young's modulus, has attracted much interest in various applications.[7,8] Especially in LIBs, graphene combined with high lithium storage property materials, such as metal oxide,[9] metal sulfide[10–12] and so on,[13–15] are well researched to improve the electrical performance. Graphene provides continuous conductive network and keep the stability of loaded materials, leading to enhanced reversible capacity and cycle performance.

Currently, chemical doping of graphene, such as B,[16] N,[17] gas,[18] metal,[19] or organic molecules,[20] is an effective approach to tailor the electronic properties and chemical reactivity of graphene. Among them, N-doped graphene has attracted great attention. Compared with the pristine graphene, N-doped graphene has more activated regions, which facilitate lithium atoms to insert/extract in graphene materials.[21] In LIBs, the RGO is the predominant matrix to hybrid with other material. The weak conductivity of RGO restricts its application as current collector. The above problem of RGO can be solved by doping with N atoms, which provide more electron cloud density and conductivity. Thermal treatment,[22] plasma treatment[23] and hydrothermal treatment[24] are applied to dope N into RGO. By N doping, graphene reveals excellent performance as LIB anodes. For example, Wang *et al.*[25] prepared nitrogen-doped graphene nanosheets by heat treatment of graphite oxide under an ammonia atmosphere at 800 °C for 2 h with a nitrogen doping level of *ca.* 2%. The nitrogen-doped graphene nanosheets exhibited a high reversible capacity of 900 mA h g^{-1} at 42 mA g^{-1}. Wu *et al.*[26] synthesized high performance N-doped graphene, which showed 872 mA h g^{-1} after 30 cycles at a low current rate of 50 mA g^{-1}. It is much higher than that of the pristine graphene (638 mA h g^{-1}).

Here we report a new route to synthesize N-GO and then reduce it to N-RGO by hydrothermal method. Different from the post-synthesis treatment mentioned above, we combine N doping and the synthesis of GO in one step. The N-RGO material shows excellent reversible capacity than that of pristine-RGO. Moreover, it is convenient to be synthesized by simple reduction of N-GO. Because of high chemical activity of N-GO, it is quite easy to combine N-GO with other materials. So, the application of N-RGO can be enlarged.

The State Key Lab of High Performance Ceramics and Superfine Microstructure, Shanghai Institute of Ceramics, Chinese Academy of Sciences, 1295 Dingxi Road, Shanghai 200050, P.R. China. E-mail: jingsun@mail.sic.ac.cn; Fax: +86-21-52413122; Tel: +86-21-52414301

† Electronic supplementary information (ESI) available. See DOI: 10.1039/c4ra05544f

2. Experimental section

2.1 Preparation of N-GO

N-GO in this work was synthesized by the modified Hummers method. 1 g natural flake graphite powder (325 mesh), 0.5 g sodium nitrate and 50 mL sulfuric acid (98 wt%) were mixed at 0 °C in ice-water bath. 3 g potassium permanganate were added slowly into the solution every half an hour, three times in total. Then 1 g melamine was put into the suspended solution and the mixture was stirred continuously for 12 h at 30 °C. After that, 46 mL hot deionized water was added into the suspension dropwise. In this step, the temperature was kept at 90 °C, and maintained for 1 h. Subsequently, 20 mL of H_2O_2 (30%) was added into the suspension. And then, 30 min of ultrasonication was taken with the power of 200 W. We centrifuged the suspension to get mud-like material. The material was washed with deionized water and ethanol for several times, respectively. At last, the material was put into oven at 40 °C and maintained for several days to get the dry N-GO material. GO with adding 0.5 g, 1 g or 2 g melamine was also prepared as control samples. The three kinds of N-GO materials are labeled as N-GO-0.5, N-GO-1.5 and N-GO-2, respectively according to the melamine quantities. Besides, GO without adding melamine was also synthesized.

2.2 Preparation of N-RGO

400 mg of the as prepared N-GO were dissolved into 80 mL deionized water. The solution was transferred into 100 mL Teflon-lined autoclave and was treated by hydrothermal process at 180 °C for 6 h. And then, the product was washed with pure deionized water and ethanol for several times. After keeping dry at 60 °C overnight, N-RGO material was obtained.

2.3 Preparation of Fe_2O_3/N-RGO

200 mg of $FeCl_3$ were dissolved into 80 mL N-GO solution which was 1 mg mL^{-1}. The mixture was transferred into 100 mL Teflon-lined autoclave and was treated by hydrothermal process at 180 °C for 10 h. And then, the product was washed with deionized water and ethanol for several times. After keeping dry at 60 °C overnight, Fe_2O_3/N-RGO material was obtained. The Fe_2O_3/RGO composite was also prepared by changing N-GO with GO.

2.4 Materials characterization

The phase identification of N-GO, N-RGO, GO and RGO were performed on the powder X-ray diffraction pattern (XRD with Cu Kα irradiation). Morphological observation was carried out on transmission electron microscope (TEM, JEM-2100F at 200 kV). The X-ray photoelectron spectroscopy (XPS) data were collected on a VG SCIENTIFIC 310F in the range of 0–1350 eV with Al target. The sample was prepared by tabletting. Raman spectra were recorded on Thermo in plus laser Raman spectrometer with a 532 nm laser (9 mW). The cyclic voltammetry (CV) data were collected on a PARSTAT 2273 electrochemical work station in the range of 3–0 eV. And Nyquist plots were collected on the same work station.

2.5 Electrochemical measurements

The electrochemical experiments of N-RGO were performed using CR 2025 type coin cells. The electrodes were prepared by mixing the active materials, acetylene black, and polyvinylidene fluoride (PVDF) binder in weight ratio of 80:10:10. After that the mixtures were dissolved in *N*-methyl-2-pyrrolidone (NMP). The electrolyte used was 1 M $LiPF_6$ in a 50:50 weight ratio ethylene carbonate (EC):dimethyl carbonate (DMC) solvent. The cells were assembled in an argon-filled glovebox and galvanostatically discharged and charged using a CT 2001 battery tester.

3. Results and discussion

The outline of the strategy to synthesize N-RGO material is shown in Fig. 1. With the presence of H_2SO_4 and $KMnO_4$, graphite is expanded and meanwhile H_2SO_4 molecule inserted into the interlamination of the graphite layers. The expanded interspace between graphite layers also can accommodates $C_3H_6N_6$ molecule. After being oxidized by H_2O and H_2O_2, graphite has been changed into GO, and N atoms also connected with GO by covalent binding in graphene layers. The hydrothermal procedure compels O atoms removed from GO, in the meanwhile, some N atoms connected with O atoms disappear as well in the process.

The XRD patterns of N-GO and N-RGO are shown in Fig. 2a. And Fig. S1† reveals the XRD patterns of GO and RGO. The content of N in N-GO and N-RGO is a small quantity, it is hard to tell the differences from N-GO to GO or N-RGO to RGO. The interlayer spacing of d_{002} in N-GO (0.884 nm) is far larger than that of N-RGO (0.357 nm). The large expansion of d_{002} is ascribed to the induced O and N containing groups, which are removed a lot in the hydrothermal process. Fig. S2† shows the XRD patterns of N-GO-0.5, N-GO-1.5 and N-GO-2. The peak around 10° is the characteristic peak of GO, while peak at 26° represents the existence of graphene or graphite. In preparation

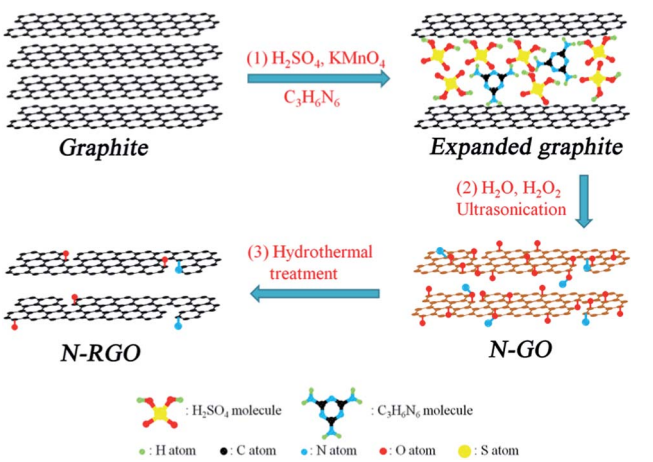

Fig. 1 Schematic diagram for the synthesis of N-RGO material.

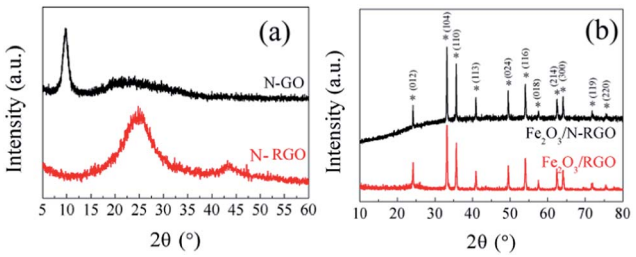

Fig. 2 XRD patterns of (a) N-GO, N-RGO and (b) Fe_2O_3/N-RGO, Fe_2O_3/RGO.

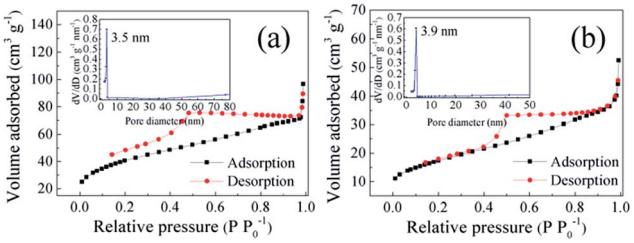

Fig. 4 Nitrogen adsorption and desorption isotherms of (a) RGO and (b) N-RGO (insert: pore diameter distribution diagram).

of N-GO-0.5, the peak in 10° is quite sharp, which means that graphite in N-GO-0.5 transforms into GO completely. When the quantity of melamine is 1.5 g, besides peak around 10° there is also a significant one around 26°. The N-GO-1.5 material has not only GO but also graphite. Too much melamine (1.5 g) in the solution could reduce the oxidation ability, resulting that graphite is hardly oxidated into GO. So, 1.5 g melamine in the experiment proves excess. The d_{002} distance in N-GO-2 even shifts to 0.828 nm, revealing that oxydic environment is weaker and more graphite remain unchanged.[27] The XRD patterns of Fe_2O_3/N-RGO and Fe_2O_3/RGO are shown in Fig. 2b. The sharp peaks in the patterns indicate that the Fe_2O_3 particles are well crystallized (JCPDS 33-0664). The peak of N-RGO is covered by the intensive Fe_2O_3 peak around 25°. Fig. S3† indicates that a lattice spacing of 0.26 nm for the (110) planes clearly identifies the Fe_2O_3 particles. The digital photograph of four kinds of N-GO materials is shown in Fig. S4.† After keeping still for 12 h, left one exhibited light yellow, leading to the best oxide GO. Left two is brown yellow, which is quite common in GO aqueous. However, left three shows almost black with a lot of graphite left in it. The left four has more graphite, even reveals poor dispersibility.

The morphology of N-GO is directly observed in the TEM images of Fig. 3. And the TEM images of GO are also shown in Fig. S5.† The surface morphology of N-GO and GO are the same by observation. And both of the two kinds of materials have wrinkled layers. It is proved that N-GO remained the 2D structure as GO.[28]

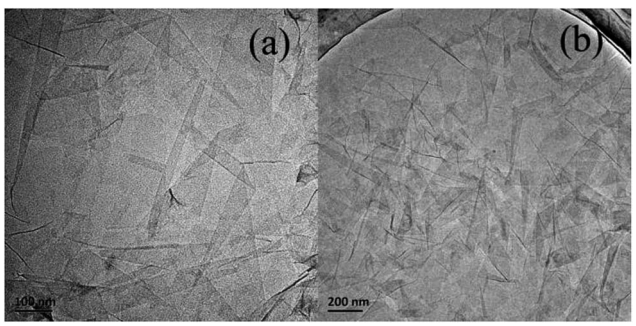

Fig. 3 TEM images of N-GO at the measuring scale of (a) 100 nm and (b) 200 nm.

Nitrogen-doping can enhance the specific surface area of graphene. Fig. 4 shows the nitrogen adsorption and desorption isotherms of RGO and N-RGO (insert: pore diameter distribution diagram). The specific surface area of N-RGO is 146.0 m^2 g^{-1}, which is much higher than that of RGO (62.4 m^2 g^{-1}). The area decreasing is because of more wrinkles and defects by nitrogen-doping. RGO and N-RGO both show IV type adsorption and desorption isotherms. It is the existence of mesopores in the materials. The hysteresis loops in them are both H2 type revealing the uniform defects in RGO and N-RGO. However, the defect size of N-RGO is 3.9 nm, a little bit larger than RGO (3.4 nm). The nitrogen atoms have the effect of enlarging the defects.

To confirm N-doping of RGO, XPS studies are carried out. The survey scan spectrum from XPS analysis shows the presence of C, N and O (Fig. 5a). And the XPS spectrum of N-GO is also shown in Fig. S6.† The O peak around 530 eV decreases obviously from N-RGO to N-GO. Table 1 supplies some element content data of N-GO, N-RGO, GO and N-GO-0.5. The O content data of N-RGO and N-GO also prove that after hydrothermal treatment, the O percentage decreased from 35.0 wt% to 11.0 wt%. In the C 1s spectrum of N-RGO in Fig. 5b, the sharp peak at

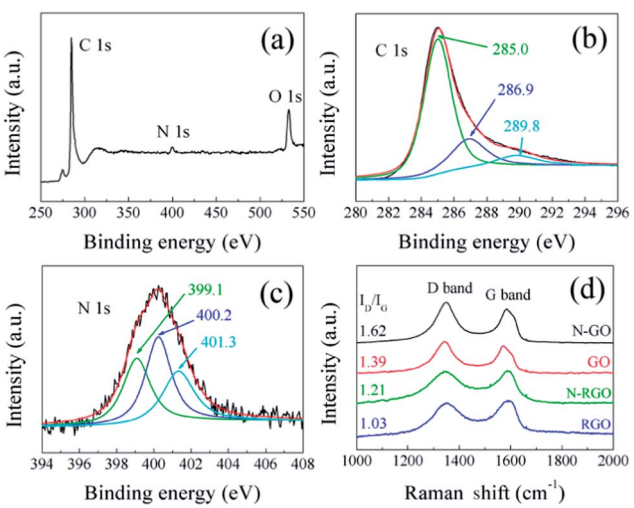

Fig. 5 (a) XPS spectrum, (b) C 1s XPS spectrum and (c) N 1s XPS spectrum of N-RGO. The N 1s peak of N-RGO can be split to three Lorentzian peaks at 401.3, 400.2, and 399.1 eV, which represent the graphitic-like nitrogen, pyrrolic-like nitrogen and pyridinic-like nitrogen species. (d) Raman spectra of N-GO, GO, N-RGO and RGO.

Table 1 Element content of C, O and N estimated from XPS data and the N/C atom ratios

Samples	C (wt%)	O (wt%)	N (wt%)	N/C (at./at.)
N-GO	59.4	35.0	5.6	0.094
N-RGO	87.0	11.0	2.0	0.023
GO	63.6	36.2	0.2	0.003
N-GO-0.5	62.0	37.7	0.3	0.005

around 286 eV can be spilt to three peaks, at 285.0, 285.9, and 289.8 eV, which represent the C=C bonds, C–O bonds and C=O bonds. Compared with C 1s XPS spectrum of N-GO which is shown in Fig. S7,† the peak of C–O bonds decreases apparently. It means that the hydrothermal treatment is effective in removing the C–O bonds.[29] The N 1s spectrum (Fig. 5c) usually can be divided to several individual peaks that are assigned to pyridinic-like N (399.1 eV), pyrrolic-like N (400.2 eV) and graphitic-like N (401.3 eV).[30,31] The N content of N-GO reaches 5.6 wt%, which is much larger than that of GO (0.2 wt%) without N-doping. When using 0.5 g melamine in N-GO-0.5 the N containing of 0.3 wt% is also quite low, which reveals that the quantity of 0.5 g melamine almost enhances no N atom doping in GO. When 1.0 g melamine used, the N content in N-GO and in N-RGO are 5.6 wt% and 2.0 wt%, respectively. We consider the N doping reaction as a concentration-dominated reaction. When added 0.5 g melamine in the solution, strong oxide environment inhibited the doping reaction, resulting rarely N doping. While 1 g melamine added, the concentration reached the necessary doping condition, leading to a high N doping content. Raman spectroscopy is another very useful method to characterize N-RGO. In Fig. 5d, the D band at 1350 cm^{-1} reveals the defects and heteroatoms, while the G band at 1580 cm^{-1} represents the ordered degree in graphene. According to the strong intensity of D peaks, the N-GO we prepared is multilayered.[32] The intensity ratio of D and G bands (I_D/I_G) is applied to describe the doping or defects phenomenon in graphene.[33] The ratios from N-GO (1.62) to N-RGO (1.21) and GO (1.39) to RGO (1.03) decrease, which can be ascribe to the reducing of O-containing group from graphene. The N-doping also make the I_D/I_G ratio lessen, compared with N-GO and GO or N-RGO and RGO. The decreased ratios also confirm the existence of N atoms doped in the graphene.

N-RGO and RGO materials are assembled in LIBs to test their electrical performances. Fig. 6 shows the Nyquist plots of the cells with N-RGO and RGO as anodes at a discharged potential of 0.1 V. It can be found clearly that the two Nyquist plots are composed of two parts, one semicircle and one straight line. The semicircle in the high frequency region is related to charge-transfer process occurring at the electrode/electrolyte interface, the straight line in the low frequency region can be attributed to Warburg impedance.[34] It is usually considered that the charge-transfer resistance can be signified by the semicircle in the medium-frequency region.[35] Although the materials are combined with carbon black (as conductive additive), it is obviously that the existence of N atoms (20 Ω of N-RGO) improves the conductivity of RGO (40 Ω of RGO). The excellent conductivity of N-RGO can arouse long cycle lifetime in high rate current density.

The cyclic voltammetry (CV) curves of N-RGO are shown in Fig. 7a. In the first cycle, the cathodic peak around 0.1 V represents the gradual insertion by lithium atoms into RGO. Meanwhile, the anodic peak presented at 0.3 V represents the extraction reaction of lithium.[30] The anodic peak shifts to 0.1 V in the second cycle because of the irreversible phase transformation in the first cycle which was resulted from the decomposition of electrolyte and formation of solid electrolyte interface (SEI).[36] Such SEI layer usually happens in the LIB anodes in the first cycle.[37] After the second cycle, the intensity of the cathodic and anodic peaks just decreases a little compared with the fifth cycle, indicating excellent cycling performance. The charge/discharge curves of N-RGO at a current density of 0.1 C are revealed in Fig. 7b. It is the voltage *versus* specific capacity plots conducted at 0.1 C between 3 and 0 V *versus* Li/Li^+. The first discharge curve at ~0.6 V can be attributed to the formation of SEI layers on the graphene surface. In the subsequent cycles, this discharge plateau disappeared. And the sloping charge/discharge curves at ~0.1 V can be attributed to

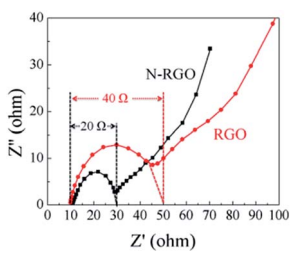

Fig. 6 Nyquist plots of N-RGO and RGO at a discharged potential of 0.1 V (*vs.* Li/Li^+) from 100 kHz to 10 mHz.

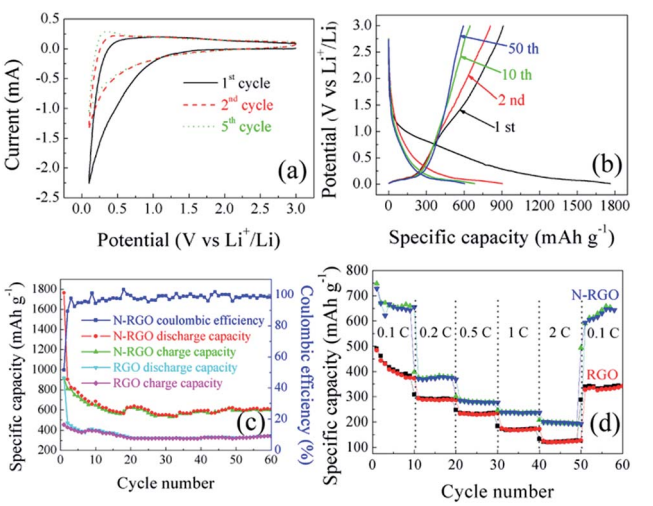

Fig. 7 (a) Cyclic voltammograms of N-RGO for the first, second, and fifth cycles at a scan rate of 0.5 mV s^{-1} with a voltage window from 3 to 0 V. (b) Lithium insertion/extraction properties of N-RGO. (c) The coulombic efficiency of N-RGO and the cycling performance of N-RGO and RGO at a current density of 0.1 C. (d) The reversible capacity of N-RGO and RGO at various current rates.

the insertion of lithium between N-RGO layers. There is no obvious decrease after the tenth cycling curve, revealing improved cycling stability. Fig. 7c shows the coulombic efficiency of N-RGO and the cycling performance of N-RGO and RGO at a current density of 0.1 C. The initial discharge and charge capacities of the composite are 1765 and 912 mA h g^{-1}, respectively, resulting in that the first coulombic efficiency is ~52%. N-RGO has higher chemical activity, leading to react with lithium ions more easily and sufficiently. Besides, there are more defects in N-RGO and lithium ions can be stored in such areas. The huge transferred lithium ions will arouse the extremely large 1st discharge capacity. The large irreversible capacity during the 1st discharge is caused by thick SEI layer. The SEI layer in N-RGO is thicker than any other materials. As a result, the irreversible capacity is larger. N-RGO has high activity and in the surface, lithium ions can react with N-RGO easily to form the SEI layer. Additionally, more defects bring N-RGO more surface areas to expose in the electrolyte, which is also aggravating the formation of SEI layer.[38] After the second cycle, the coulombic efficiency of N-RGO remains above 95%. After 60 cycles, N-RGO can deliver a reversible capacity of 600 mA h g^{-1}. While the RGO for comparison shows only 350 mA h g^{-1}. The increased percentage of capacity reaches as high as 71.4%. The rate performance of the N-RGO electrode is investigated in Fig. 7d. At a current density of 2 C, the discharge/charge capacity of N-RGO still remains ~200 mA h g^{-1}, while that of RGO is only ~120 mA h g^{-1}. The N-RGO exhibits higher reversible capacity both at low and high current densities. To better understand the advantage of nitrogen-doping in RGO, the cycling performances of Fe_2O_3/N-RGO and Fe_2O_3/RGO at a current density of 100 mA h g^{-1} were exhibited in Fig. 8. After 50 times the revisable capacity of Fe_2O_3/N-RGO remains as high as ~1050 mA h g^{-1}, which is higher than the ~700 mA h g^{-1} of Fe_2O_3/RGO. When Fe_2O_3 loaded on the surface of N-RGO, the surface will be covered and electrolyte will not contact with N-RGO sufficiently in the first few cycles, and in long time cycling the advantages of N-RGO than RGO could be more obvious and hence initial capacity is close and several cycles later the capacities make obviously different. In the composite of Fe_2O_3/NRGO, Fe_2O_3 mainly store lithium ions. When lithium ion batteries discharge, lithium ions will react with Fe_2O_3 and deliver the reversible capacity. N-RGO shows higher conductivity than RGO and lithium will travel faster in N-RGO than RGO, resulting higher capacity. The outstanding properties of N-RGO can also facilitate the composite which contain N-RGO.

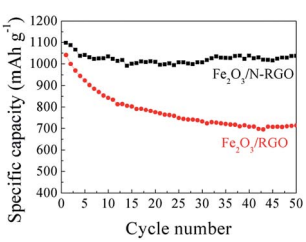

Fig. 8 The cycling performances of Fe_2O_3/N-RGO and Fe_2O_3/RGO at a current density of 100 mA h g^{-1}.

4. Conclusions

We invent a new method to synthesize nitrogen-doped reduced graphene oxide (N-RGO) with excellent lithium storage properties. N doping is concurrent in the formation of GO. We also have discussed the quantity of N-GO with different quantities of melamine. Nitrogen content of N-GO can reach up to 5.6 wt%. After reduction, the nitrogen content of N-RGO still remains 2.0 wt%. The N-RGO material shows excellent reversible capacity of 600 mA h g^{-1} at a current density of 0.1 C after 60 cycles, superior to that of pristine-RGO (350 mA h g^{-1}). As it is known, the conductivity of anode materials plays an important role in electron transmission, especially in high rate current density. By doping N atoms, the charge-transfer impedance of N-RGO (20 Ω) decreases a half than that of RGO (40 Ω). In the charge process, lithium ions diffuse into the anode materials and the higher conductivity facilitate faster ions diffusion, leading to higher specific capacity. Besides, the defects and disordered surface morphology induced by doping, increase electrode/electrolyte wettability and improve electrochemical performance. Notably, N atoms play an effective role in lithium intercalation and extraction, making the process much easier. This work opens up a new way to synthesize N-RGO, which is a promising candidate for lithium ion battery (LIB) anodes whether be used alone or combined with other materials.

Acknowledgements

This work is supported by the National Basic Research Program of China (2012CB932303) and the National Natural Science Foundation of China (Grant no. 51072215 and 51172261).

Notes and references

1 M. Armand and J. M. Tarascon, *Nature*, 2008, **451**, 652–657.
2 R. Mukherjee, A. V. Thomas, A. Krishnamurthy and N. Koratkar, *ACS Nano*, 2012, **6**, 7867–7878.
3 K. Kang, *Science*, 2006, **311**, 977–980.
4 X. Zhu, Y. Zhu, S. Murali, M. D. Stoller and R. S. Ruoff, *ACS Nano*, 2011, **5**, 3333–3338.
5 D. W. Kim, Y. D. Ko, J. G. Park and B. K. Kim, *Angew. Chem., Int. Ed.*, 2007, **46**, 6654–6657.
6 X. Yinglin, Z. Jiantao, T. Liqi, L. Bo, H. Qianyan, Y. Chao and Q. Xuefeng, *Phys. Chem. Chem. Phys.*, 2013, **15**, 3939–3945.
7 A. A. Balandin, S. Ghosh, W. Z. Bao, I. Calizo, D. Teweldebrhan, F. Miao and C. N. Lau, *Nano Lett.*, 2008, **8**, 902.
8 C. Lee, X. Wei, J. W. Kysar and J. Hone, *Science*, 2008, **321**, 385–388.
9 X. Wei, W. Zhixing, G. Huajun, L. Xinhai, W. Jiexi, H. Silin and G. Lei, *Appl. Surf. Sci.*, 2013, **266**, 148–154.
10 G. Yan, X. Yi and W. Yong, *ACS Appl. Mater. Interfaces*, 2013, **5**, 801–806.
11 X. Zhou, L. J. Wan and Y. G. Guo, *Chem. Commun.*, 2013, **49**, 1838–1840.
12 X. Wei, W. Zhixing, G. Huajun, Z. Yunhe, Z. Qian and G. Lei, *J. Alloys Compd.*, 2013, **560**, 208–214.

13 M. Zhou, T. Cai, F. Pu, H. Chen, Z. Wang, H. Zhang and S. Guan, *ACS Appl. Mater. Interfaces*, 2013, **5**, 3449–3455.
14 G. Mingyuan, R. Jiepeng, F. Xin, Z. Anyi, L. Yunhao and Z. Chongwu, *Nano Res.*, 2013, **6**, 174–181.
15 B. Wang, X. Li, X. Zhang, B. Luo, M. Jin, M. Liang, S. A. Dayeh, S. T. Picraux and L. Zhi, *ACS Nano*, 2013, **7**, 1437–1445.
16 W. Huan, Z. Yu, W. Di, L. Lei, Z. Shuli, P. Hailin and L. Zhongfan, *Small*, 2013, **9**, 1316–1320.
17 D. Yu, L. Wei, W. Jiang, H. Wang, B. Sun, Q. Zhang, K. Goh, R. Si and Y. Chen, *Nanoscale*, 2013, **5**, 3457–3464.
18 F. Schedin, A. K. Geim, S. V. Morozov, E. W. Hill, P. Blake, M. I. Katsnelson and K. S. Novoselov, *Nat. Mater.*, 2007, **6**, 652–655.
19 G. Giovannetti, P. Khomyakov, G. Brocks, V. Karpan, J. van den Brink and P. Kelly, *Phys. Rev. Lett.*, 2008, **101**, 026803.
20 W. Chen, S. Chen, D. C. Qi, X. Y. Gao and A. T. S. Wee, *J. Am. Chem. Soc.*, 2007, **129**, 10418–10422.
21 C. Y. Jae, K. H. Sung, I. Hyungsoon, M. Yoon, J. G. Bok, L. C. Woo, P. Jeunghee, P. Mi-Hee, C. Jaephil and K. H. Seok, *J. Phys. Chem. C*, 2011, **115**, 9451–9457.
22 C. Dandan, L. Dongdong, W. Suqing, Z. Xuefeng, Y. Weishen, Z. Shanqing and W. Haihui, *J. Alloys Compd.*, 2013, **561**, 54–58.
23 H. M. Jeong, J. W. Lee, W. H. Shin, Y. J. Choi, H. J. Shin, J. K. Kang and J. W. Choi, *Nano Lett.*, 2011, **11**, 2472–2477.
24 S. Yang, X. Song, P. Zhang and L. Gao, *ACS Appl. Mater. Interfaces*, 2013, **5**, 3317–3322.
25 W. Haibo, Z. Chuanjian, L. Zhihong, W. Li, H. Pengxian, X. Hongxia, Z. Kejun, D. Shanmu, Y. Jianhua and C. Guanglei, *J. Mater. Chem.*, 2011, **21**, 5430–5434.
26 Z.-S. Wu, W. Ren, L. Xu, F. Li and H.-M. Cheng, *ACS Nano*, 2011, **5**, 5463–5471.
27 S. Guido, P. Tobias, K. Richard, F. Olga, M. Hinrich-Wilhelm, P. Stefano and W. Martin, *J. Power Sources*, 2013, **239**, 563–571.
28 Z. C. Wang Haibo, L. Zhihong, W. Li, H. Pengxian, X. Hongxia, Z. Kejun, D. Shanmu, Y. Jianhua and C. Guanglei, *J. Mater. Chem.*, 2011, **21**, 5430.
29 Z.-H. Sheng, L. Shao, J.-J. Chen, W.-J. Bao, F.-B. Wang and X.-H. Xia, *ACS Nano*, 2011, **5**, 4350–4358.
30 A. L. M. Reddy, A. Srivastava, S. R. Gowda, H. Gullapalli, M. Dubey and P. M. Ajayan, *ACS Nano*, 2010, **4**, 6337–6342.
31 X. Li, H. Wang, J. T. Robinson, H. Sanchez, G. Diankov and H. Dai, *J. Am. Chem. Soc.*, 2009, **131**, 15939–15944.
32 Y. Zhu, S. Murali, W. Cai, X. Li, J. W. Suk, J. R. Potts and R. S. Ruoff, *Adv. Mater.*, 2010, **22**, 3906–3924.
33 L. Dan, S. Dongqi, C. Zhixin, L. Huakun, J. Dianzeng and G. Zaiping, *RSC Adv.*, 2013, **3**, 5003–5008.
34 T. Qiwei, S. Zhongqiang, W. Li and Q. Xue, *Electrochim. Acta*, 2012, **79**, 148–153.
35 Z. Mei and J. Mengqiu, *J. Alloys Compd.*, 2013, **551**, 53–60.
36 B. P. Vinayan and S. Ramaprabhu, *J. Mater. Chem. A*, 2013, **1**, 3865–3871.
37 X. Zhou, L. J. Wan and Y. G. Guo, *Adv. Mater.*, 2013, **25**, 2152–2157.
38 L. Su, Y. Zhong and Z. Zhou, *J. Mater. Chem. A*, 2013, **1**, 15158.